JOURNAL OF
ELECTRON SPECTROSCOPY
and Related Phenomena

ELSEVIER Journal of Electron Spectroscopy and Related Phenomena 84 (1997) 53–72

X-ray spectromicroscopy of polymers and tribological surfaces at beamline X1A at the NSLS

H. Ade[a,*], A.P. Smith[a], H. Zhang[a], G.R. Zhuang[1a], J. Kirz[b], E. Rightor[c], A. Hitchcock[d]

[a] *Physics Department, North Carolina State University, Raleigh, NC 27695-8202, USA*
[b] *Physics Department, SUNY@Stony Brook, Stony Brook, NY 11794, USA*
[c] *Texas Polymer Center, B-1470, Dow Chemical, Freeport, TX 77541, USA*
[d] *Brookhouse Institute for Materials Research, McMaster University, Hamilton, ON L8S 4M1, Canada*

Received 2 July 1996; accepted 3 December 1996

Abstract

We provide a general overview of microspectroscopy and spectromicroscopy for materials characterization at beamline X1A at the national synchrotron light source (NSLS). Two instruments, the scanning transmission X-ray microscope (STXM) and scanning photoemission microscope (SPEM), are available. The STXM has been able to provide a spatial resolution of better than 50 nm for several years and near edge X-ray absorption fine structure (NEXAFS) spectroscopy is performed in transmission from thin samples at an energy resolution of typically 0.3 eV at the carbon K-edge. Numerous applications in polymer science and biology have been performed to date. We restrict our review to polymer science applications and present new results of several polymer systems. The SPEM has a spatial resolution of about 250 nm in routine operation and was recently upgraded with a hemispherical sector analyzer to improve the data throughput. We present the latest SPEM results, which were generated from a tribological sample. © 1997 Elsevier Science B.V.

Keywords: Polymers; Tribology; X-ray microscopy; NEXAFS; XPS; Spectroscopy

---

1. Introduction

1.1. X-ray microscopy at the national synchrotron light source (NSLS)

X-ray microscopy at the NSLS (a list of acronyms can be found in Table 1) has been pursued for more than 15 years. At that time, a group from SUNY@ Stony Brook began to develop a scanning transmission X-ray microscope (STXM) that made use of bending magnet radiation [1]. This activity has since moved to using the X1A undulator beamline for an STXM developed primarily by Stony Brook [2,3] and a scanning photoemission microscope (SPEM) developed by North Carolina State University (NCSU) and Stony Brook. X-ray microscopy applications have emphasized imaging of biological materials at photon energies in the so-called water window between the carbon K-edge at 290 eV and the oxygen K-edge at 540 eV. Carbon is highly absorbing at these energies while oxygen is not, and these energies thus provide high contrast between carbon-based biological materials in aqueous solutions. To some extent, this is the simplest form of spectroscopic

---

* Corresponding author. Phone: +1 919 515 1131; fax: +1 919 515 4496; e-mail: harald_ade@ncsu.edu

[1] Present address: LBNL, Berkeley, CA, USA.

PII S0368-2048(97)00013-3

Table 1
Acronyms

ABS	Acrylonitrile–butadiene–styrene
AFM	Atomic force microscopy
AN	Acrylonitrile
BNL	Brookhaven National Laboratory
CMA	Cylindrical mirror analyzer
EELS	Electron energy loss spectroscopy
EM	Electron microscopy
FWHM	Full width at half maximum
HSA	Hemispherical sector analyzer
IR	Infrared
LCP	Liquid crystalline polymer
LDPE	Low-density polyethylene
LFM	Lateral force microscopy
MCD	Multichannel detector
MDI	Methylene diphenyldiisocyanate
NEXAFS	Near edge X-ray absorption fine structure
NMR	Nuclear magnetic resonance
NSLS	National synchrotron light source
Nylon 6	Poly(ϵ-caprolactam)
OP	Orientation parameter
OSA	Order-selecting aperture
PAR	Polyarylate
PB	Polybutadiene
PC	Polycarbonate
PE	Polyethylene
PET	Poly(ethylene terephthalate)
PP	Polypropylene
PPTA, Kevlar®	Poly(*p*-phenylene terephthalamide)
PS	Polystyrene
SAN	Styrene–acrylonitrile
SPEM	Scanning photoemission microscope/ microscopy
STXM	Scanning transmission X-ray microscope/ microscopy
TDI	Toluenediisocyanate
UHV	Ultra-high vacuum
X1-SPEM	Scanning photoemission microscope at beamline X1 at NSLS
X1-STXM	Scanning transmission X-ray microscope at beamline X1 at NSLS
XANES	X-ray absorption near edge structure
XPS	X-ray photoelectron spectroscopy
ZP	Zone plate

imaging as the contrast depends on the electronic structure of the sample constituents. Elemental mapping of calcium in biological materials utilizing the Ca $L_{II,III}$-edge near 348 eV was subsequently developed [4]. To date, biology-related efforts at X1A still far outweigh and outnumber materials characterization efforts [5].

From the beginning, a scanning geometry had been chosen for the lowest possible exposure to the sample. In the transmission X-ray imaging geometry [5] the inefficient (about 10–20%) optical element—a zone plate—is between the sample and the detector, while in the scanning geometry the zone plate is upstream of the sample, and there is only a small He-filled gap between the sample and the detector. Scanning instruments thus offer a reduced exposure of a factor of 5–10 in most implementations of these complementary X-ray microscopy schemes. The additional exposure factor in the imaging transmission geometry is E_a/100%, where E_a is the absolute (including substrate) first-order diffraction efficiency of the zone plate. E_a is typically well below 20%. Hence, the scanning geometry is best suited to investigate radiation-sensitive materials such as biological samples and polymers. As it turned out in the early 1990s, more than a decade after it was decided to exploit the scanning geometry, the STXM had the added benefit of being more readily adapted for more sophisticated microspectroscopy and spectromicroscopy techniques than would have been possible with an imaging geometry microscope. This dual advantage was rapidly exploited for both polymer and biology applications once the X1-STXM was operated as a near edge X-ray absorption fine structure (NEXAFS) microscope.

The first specific spectromicroscopy program at beamline X1A aimed at achieving chemical state information at high spatial resolution was started in the late 1980s with the development of an SPEM [6]. It was based on zone plate optics and a cylindrical mirror analyzer (CMA) in an ultra-high vacuum (UHV) chamber and was intended to investigate surfaces. Although it had a rather modest energy resolution of about 4–7 eV, this SPEM was the first spectromicroscope to achieve submicron X-ray photoelectron spectroscopy (XPS) microscopy, mapping oxidation states of silicon with a spatial resolution of about 500 nm [7]. The spatial resolution was subsequently improved to about 150 nm [8]. At about the time of breaking the micron barrier in XPS, Tonner's group had achieved the first submicron X-ray absorption near edge structure (XANES) microscopy from surfaces with electrostatic imaging techniques [9,10]. The X1-STXM was utilized to achieve XANES imaging in transmission at 30–50 nm spatial resolution in 1992 [11]. The project MAXIMUM subsequently pushed the spatial resolution limit of XPS spectromicroscopy to about 100 nm [12]. Recently, Bauer's group reported having achieved a spatial resolution of about 40 nm in the XPS mode [13]. Out of the developments mentioned here, we will detail the contributions of the zone plate-based instruments at beamline X1A and provide various examples for their applications. There are, of course, also spectromicroscopy efforts not mentioned here that have evolved concurrently. We assume that a recent, complete and complementary perspective to that provided in this short introduction and in this article will be offered by other contributions to this special issue and we will not attempt to provide a complete overview of the field.

1.2. Motivation: NEXAFS spectroscopy of polymers as an example

While providing a general motivation for X-ray spectromicroscopy in an article in this issue might appear superfluous, we would nevertheless like to provide a specific motivation for some of the developments at beamline X1A. Much of the analytical characterization potential of X-ray microscopy rests on the semiquantitative chemical fingerprinting capability of X-ray absorption spectroscopy and the quantitative chemical analytical capabilities of XPS. The capabilities of XPS are well known and we will focus our attention on absorption spectroscopy. In absorption spectroscopy one measures the absorption cross-section in the vicinity of core shell absorption edges as a function of photon energy. The details of the spectral features obtained reveal the element-specific, local unoccupied electronic structure of the system under study in the presence of a core hole. This spectral signature is referred to as near edge X-ray absorption fine structure (NEXAFS), or X-ray absorption near edge structure (XANES). An excellent monograph and introduction to the subject for NEXAFS spectroscopy in the soft X-ray range for small molecules and polymers (without spatial resolution) is available [14]. Due to the requirement of photon tunability and high intensity, most, if not all, NEXAFS experiments are performed at synchrotron radiation facilities. These sources provide broad band or tunable radiation that is linearly polarized in the plane of the electron storage ring. Applications of NEXAFS spectroscopy include identification of specific functional groups in polymers, determination of the orientation of small molecules and polymers, and characterization of the oxidation states in metals.

For organic molecules and polymers, NEXAFS is most sensitive to differentiate saturated from unsaturated bonding. It is core excitations into unoccupied π^* orbitals that result in the most narrow and intense NEXAFS features. These π^* transitions are characteristic of unsaturated bonding. In order to illustrate the capabilities of NEXAFS we will compare the NEXAFS spectra of various polymers in Fig. 1. These spectra have been acquired with the X1-STXM from thin sections (100–200 nm thick) with an energy resolution of about 0.3 eV. We have chosen polystyrene (PS), poly(ethylene terephthalate) (PET), polycarbonate (PC), polyarylate (PAR), polypropylene (PP), polyethylene (PE) and poly(*p*-phenylene terephthalamide) Kevlar® as examples. As can be readily observed, the spectra of all polymers containing unsaturated bonds are substantially different from saturated polymers such as PE and PP. Typically, the lowest excitation energy corresponding to double (or triple) carbon–carbon bonds without heteroatoms as nearest neighbors is near 285 eV. A good example of that is the spectrum of PS, which has an intense peak at 285 eV. Additional features in the PS spectrum correspond to the $2\pi^*$ transition at 288.8 eV and σ^* transitions at 287.2 (C–H) and 295 eV (C–C) [14]. In PS all six carbon atoms are nearly equivalent and contribute to the π^* peak near 285 eV. However, in other polymers such as PC, PET and Kevlar®, the substitutional carbon atom of the phenylene differs from the other carbon atoms in the ring, which causes the peak near 285 eV to split. For example, the peak at 286.1 eV of Kevlar® corresponds to core excitations from phenylene carbon atoms which are next to amide groups while some carbon atoms of the phenylene in PC are next to an ether linkage and correspond to transitions at 286.8 eV. Many times these shifts occur because of shifts in the initial core electron binding energy due to the larger electronegativity of the heteroatom, but site-specific relaxation (the response of the electronic system to the core hole disturbance) plays a crucial role in determining the precise energy and the intensity of the transition. Furthermore, considerable delocalization of the π orbitals can occur on conjugated moieties. This causes π^* energy levels to split, and the splitting of the

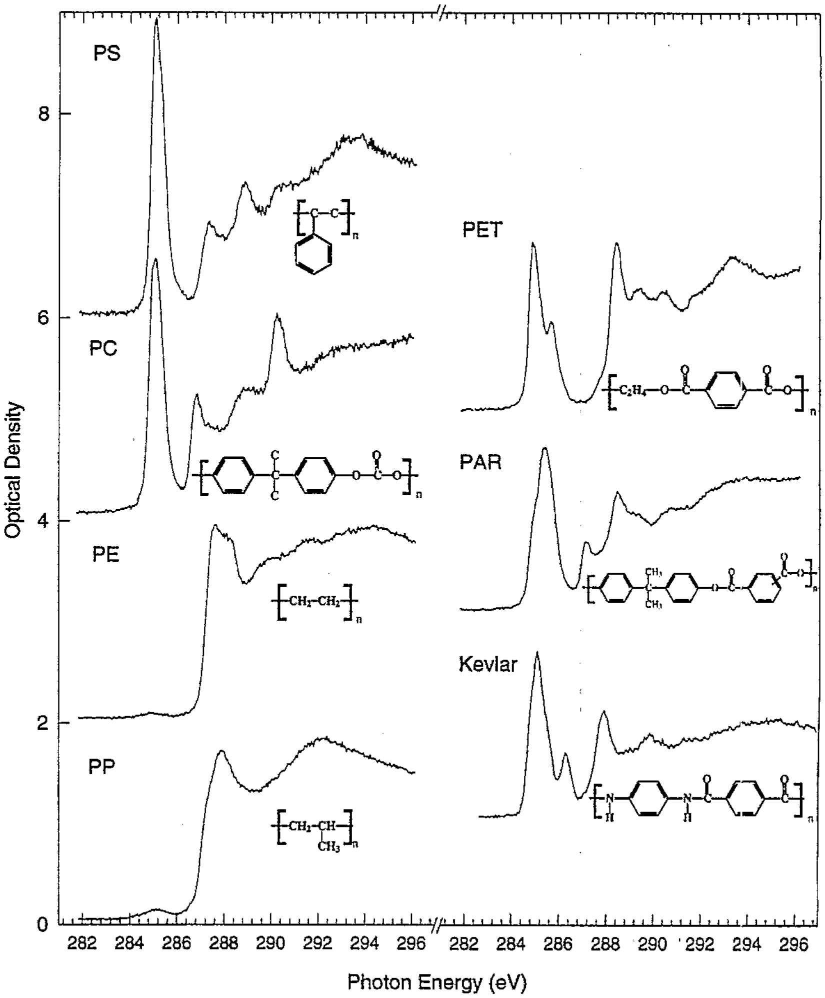

Fig. 1. NEXAFS spectra of PS, PC, PE, PP, PET, PAR and Kevlar® acquired with the X1-STXM at an energy resolution of about 0.3 eV.

aromatic π^* transitions of PET around 285 eV is a good example [15]. Conjugation and delocalization is also the reason for the $2\pi^*$ (288.8 eV) transition in PS. Thus, the NEXAFS spectra depend not only on the presence of certain bonds, heteroatoms, functional groups or moieties, but also on their configuration and interaction. If there is no interaction between various moieties, a ''building block'' approach to NEXAFS spectroscopy is quite successful. The NEXAFS spectrum of a material composed of various ''building blocks'' can then be considered as the weighted linear combination of the NEXAFS spectra of each component or ''building block''. This approach is at least semiquantitative and can be utilized for analysis of complex materials of unknown composition for which some guiding information or core excitation spectra of molecular analogs or other ''building blocks'' have already been recorded. A set of NEXAFS spectra of polymers complementary to those presented here can be found in an article by Kikuma and Tonner [16] and in [14].

While saturated versus unsaturated bonding and the presence of heteroatoms produce large NEXAFS differences, it is interesting to compare the NEXAFS spectra of two saturated polymers to provide a sense of the sensitivity of the technique where one would expect relatively small spectral differences. PP and PE, polymers that differ in the most simplistic approach primarily in their relative amounts of C–H and C–C bonds, exhibit subtle, but distinguishable, differences in their NEXAFS spectra as can be seen from the spectra displayed in Fig. 1. Polarization-dependent NEXAFS spectra of oriented PE and related alkyl hydrocarbons show a marked sensitivity to the orientation with respect to the polarization vector [14,17,18]. We believe there is no orientational order in the PP and PE investigated with the X1-STXM and the observed spectral differences are solely chemical in nature. The beam was highly defocused during spectral acquisition. The bumps near 285 eV should not be there and are most likely not due to radiation damage but some minority chemical component.

Interesting differences in core-excitation spectra have also been recorded for ortho, meta and para substitutional sites in various small molecules and oligomers [19,20]. This sensitivity to substitutional isomerism is also reflected in the differences between the PAR, PET and PC spectra. Based on a ''building block'' approach, one would think that the energies of the spectral features of PAR would be a combination of those found in PET and PC, except for the carbonyl peak in PC. Fitting of the PAR spectrum requires, however, different energy values and intensities for the peaks than those found in PET and PC, even near 285 eV. This is most likely due to the fact that the PAR material has 50/50 meta/para substitution, while PET and PC have 100% para substitutional sites. In general, the coupling of molecular orbitals within the terephthalate group is quite different for meta and para substitutions [20]. This extraordinary sensitivity can be put to great use in NEXAFS microscopy to locate a specific component or to analyze an unknown material into its majority components. Unfortunately, all the spectral features in NEXAFS are bunched up right near the edge. In the most general case it will thus be difficult to determine minority species in multicomponent, homogenous materials, at least when using only core edges dominated by the majority component.

2. X-ray optics of the X1-STXM and X1-SPEM

Although the X1-STXM [2,3], X1-SPEM [21] and the X1A beamline [22] have been described elsewhere in detail, we will discuss some of the most important features to convey the strengths and weaknesses of the zone plate-based approach to spectromicroscopy and to understand present limitations of the X1A spectromicroscopy program. The X1-STXM has at its heart a focusing optical element, a zone plate, that has to be coherently illuminated to provide the highest spatial resolution possible. Given this constraint, only undulator sources at high brightness storage rings and their associated monochromator beamlines result in small microprobes of sufficient intensity to perform experiments. In addition, zone plates are based on diffractive optical principles—they have alternating ''opaque'' and transparent zones—and only a small fraction of the usable intensity is diffracted into the positive first order that is utilized for microprobe formation. All other orders have to be eliminated with an order-selecting aperture (OSA) to achieve high signal-to-background (S/B) ratios (for a schematic see Fig. 2). Presently, the highest resolution zone plates at X1A have a diameter of 80–90 μm, an outermost zone width of 30–45 nm, and hence a focal length of less than 1 mm at 280 eV. Due to the OSA the usable working distance is reduced to less than 200 μm. The focal length f of a zone plate is furthermore proportional to the photon energy E ($f \propto E$), which requires that the instrument be refocused if absorption spectra are to be acquired from the smallest possible spot.

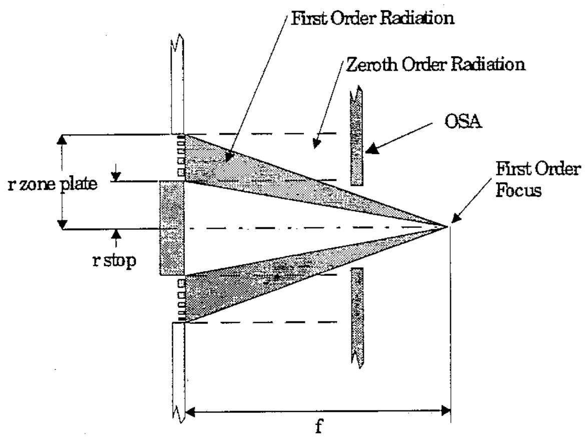

Fig. 2. Schematic of zone plate (ZP) optics and pinhole suppressing unwanted diffraction orders (order-selecting aperture, OSA). Note that only zero and first order are shown.

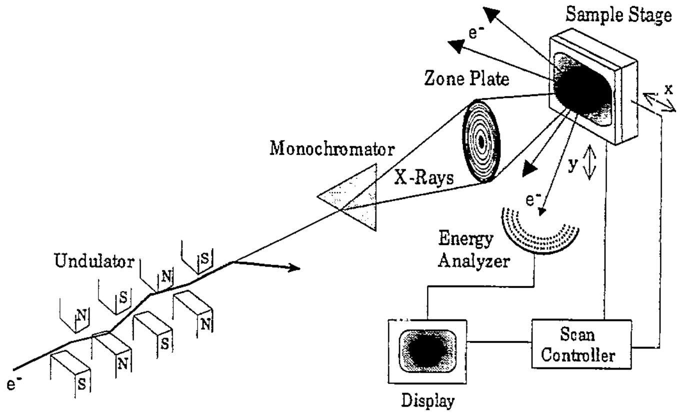

Fig. 3. Schematic representation of the X1-SPEM-II in XPS detection mode. Other possible but only partially implemented detection modes are the various NEXAFS modes (total electron yield, Auger electron yield, fluorescent yield), transmission and luminescence spectroscopy. (Note that the energy analyzer is a hemispherical sector analyzer.)

The basic optical concepts of the X1-SPEM are the same as those of the X1-STXM, except that photoelectrons are energy analyzed with conventional spectrometers in a "back-reflection" geometry to provide spectroscopic information (see Fig. 3). This makes it even more difficult to operate with the small working distances provided by zone plates. Typically, the zone plate parameters in the X1-SPEM are thus somewhat relaxed and zone plates with larger outermost zone widths Δd, and therefore worse spatial resolution, are utilized. Larger Δd values put less stringent requirements on the zone plate fabrication process and allow larger zone plates to be fabricated. Both aspects, larger diameter d and larger Δd, provide longer focal lengths f, since $f = d \times \Delta d/\lambda$, where λ is the photon wavelength. (The zone plates utilized in the X1-STXM and X1-SPEM have been fabricated by E. Anderson from the Center for X-ray Optics in a collaboration with IBM Yorktown Heights.) Presently, the zone plates utilized for the X1-SPEM-II have a diameter of 140 μm and an outermost zone width of 80 or 100 nm. The small working distance, in particular, puts constraints on the design and operation of an XPS microscope, while the necessity for refocusing in an XANES/NEXAFS mode puts extreme demands on the mechanical stages; only very small runout in the X and Y direction can be tolerated as the stages refocus in the Z direction.

The X1-SPEM shares the same monochromator that provides beams for the X1-STXM in a "duochromator" scheme that has two exit slits and branchlines at different included angles. The difference in photon energy is about a factor of two to match the fundamental and second harmonic output of the X1 undulator [22]. This couples the two microscopes directly and in addition severely restricts the real estate available for SPEM instrument development due to the very small angular separation of the branchlines. In this arrangement the available energy range for the X1-SPEM is restricted to 450–750 eV and the diffraction efficiency of the monochromator is low, while the X1-STXM can operate over the 250–750 eV energy range at generally higher efficiency. The X1-STXM by and large also enjoyed the privilege of having priority of controlling the precise photon energy. While this arrangement limited progress with the X1-SPEM, it was certainly a great arrangement to have the additional, low-cost branchline to develop the X1-SPEM in the first place. Presently, two new independent beamlines, each with its own gratings and slits, are being installed at X1A in an effort to provide equal access for the X1-SPEM and X1-STXM to a resource such as the X1 undulator [23].

3. Operation of the Stony Brook STXM

We describe here the operation of the X1-STXM developed by Stony Brook [2,3] in its current configuration (a completely redesigned system is expected to begin operation in 1997). The X1-STXM is operated with the sample located in a helium-purged atmospheric pressure environment. The sample is raster scanned under computer control with capacitance-controlled piezo-transducers to acquire images. Alternatively, the X, Y position is held fixed while the photon energy and the Z position of the zone plate are scanned in synchrony to acquire an energy scan from a small spot. The transmitted flux is detected with a gas flow counter. To collect absorption spectra, an energy scan (I) from the sample is recorded, and subsequently or just prior to it another energy scan (I_0) is recorded without a sample or through an open area of the sample. The negative log ratio of these energy scans ($-\ln(I/I_0)$) is an optical density spectrum in units of absorption lengths. Typically, sections 100–200 nm in thickness are utilized for carbon K-edge NEXAFS. It takes a few minutes to acquire an image with compositional information (spectromicroscopy) and about the same time to record several energy scans from small sample areas (microspectroscopy) and normalization scans from open areas. It has to be emphasized that the present X1-STXM was not designed or engineered to perform microspectroscopy. The results achieved to date and presented below are therefore even more gratifying. The limited engineering imposes, however, some unwelcome limitations. At this point in time, for example, the helium purge of the X1-STXM enclosure is imperfect. Small and varying amounts of oxygen and nitrogen are still present which make applications near the oxygen and nitrogen K-edges essentially impossible. X1-STXM spectromicroscopy applications have therefore focused on carbon K-edge NEXAFS, even in cases where the oxygen edge would yield more science.

A small amount of CO_2 can be admixed to the helium which provides for easy characterization of the monochromator. Energy resolution, energy calibration and linearity, as well as problems with higher-order contamination, can be assessed utilizing the various Rydberg transitions and other features in the CO_2 NEXAFS spectrum. As an example, we show a CO_2 spectrum in Fig. 4(A) that has the expected π^* transition at 290.74 eV and Rydberg transitions at 292.80 eV (3s), 295.00 eV (3p) and 296.38 eV (4p) [24]. It also shows, however, a dip near 285 eV that should not be there. This is caused most likely by detector non-linearity and higher-order spectral contamination that is exacerbated by large dips in the normalizing I_0 energy scan at these energies due to carbon build-up on the beamline optics and on various membranes of the microscope traversed by the X-rays. Occasionally, we also observe a peak near 285 eV in a CO_2 NEXAFS spectrum (Fig. 4(B)). This peak occurred during a period with detector problems, although we are not sure at this point what the precise causes are. The saturation of the π^* transition can also be utilized in tests as an indication of the severity of higher-order spectral contamination. We show these results to illustrate that there is a quick and easy way to assess whether there are problems with the STXM spectral acquisition mode. This quality assurance procedure can be easily adopted in any transmission X-ray spectromicroscope. It is particularly important for quantitative analysis and to facilitate comparisons of results from data run to data run. During most of the X1-STXM operation, conditions are significantly better than those shown in Fig. 4(A) and Fig. 4(B) and the CO_2 spectra have virtually no features near 285 eV (see Fig. 4(C)). The widths of the Rydberg states can be utilized to assess the energy resolution. A simultaneous spectrum of PET and CO_2 is acquired by leaking CO_2 into the enclosure while the PET sample is in place (Fig. 4(D)) and allows direct energy calibration of the PET spectrum. It is best in that instance to highly saturate the π^* peak at 290.74 eV and use the sharper Rydberg states as energy reference. What appears to be an offset in Fig. 4(D) is due to the oxygen valence electron cross-section and the high concentration of CO_2. It is interesting to note that the π^* peak saturates at quite different optical densities in these spectra. In spectra 4(A) and 4(B) the saturation is much more pronounced than in 4(C) and 4(D) due to a higher level of spectral contamination. This elevated higher-order contamination typically coincides with spectral distortions near 285 eV.

We have only recently started to utilize this "quality assurance" procedure. It will allow one to directly couple the energy scales of various polymers (or other materials) and to assess small but real shifts of spectral features. Unfortunately, the X1 monochromator utilized for the data presented in this manuscript was not intended for spectroscopy and we find shifts and variations over time both in energy calibration and linearity. As mentioned previously, a

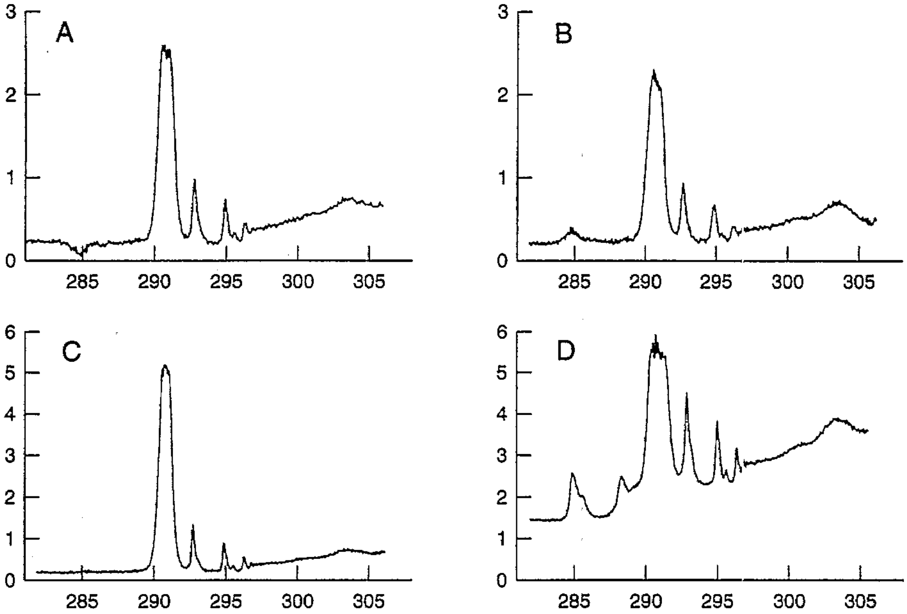

Fig. 4. CO_2 NEXAFS spectra utilized to assess the operating conditions of the X1-STXM in spectral acquisition mode (see text for discussion).

much improved monochromator with better energy resolution and energy linearity is presently being installed that should remedy these problems.

4. Material science applications of STXM

Materials science applications with the X1-STXM have so far almost exclusively focused on synthetic polymeric materials. Generally, they fall into four categories. In the first, the material is composed of a limited number of components of which reference spectra can be obtained if necessary. The objective then is to map the distribution of these components and a good guess for the best photon energies to utilize is obtained from the reference spectra. In the second category, inclusions or phases in the material have been observed with other techniques and the X1-STXM is utilized primarily in microspectroscopy mode as an analytical instrument. Model spectra from a large variety of materials are utilized to interpret and to model the spectra from the various phases. The third type of problem is one in which only limited and indirect information about the material exists and the objective is a basic characterization from scratch. This is by far the most difficult one, since little guidance is available to even decide which photon energy to use to provide good contrast for the texture of the material to be revealed. The fourth category is mostly concerned with orientational order, rather than chemical inhomogeneity, and linear dichroism microscopy and microspectroscopy are utilized to extract information concerning orientation of specific functional groups. We will subsequently describe applications that illustrate these four categories.

4.1. Polymer blends

Since NEXAFS microscopy provides direct compositional information at relatively high spatial resolution, it might be an invaluable tool to characterize multicomponent systems, such as binary, ternary or quaternary polymer blends. Traditionally, conventional microscopies, particularly electron microscopy in conjunction with staining methods, are used for the characterization of these materials. Many systems of interest contain, however, components that have very similar absorption rates for staining agents. It is then impossible to delineate these components in an electron microscope. Furthermore, there is also

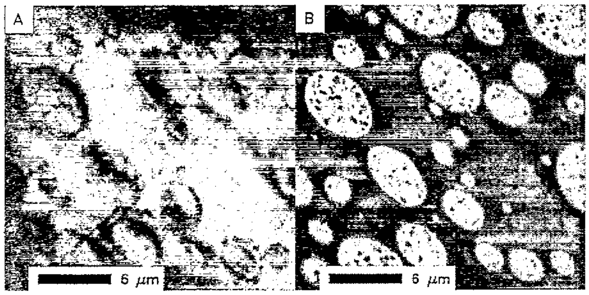

Fig. 5. Micrograph of LDPE, PET and Kraton ternary blend acquired at a photon energy of (A) 299 eV and (B) 285.1 eV. Both LDPE and Kraton appear relatively dark in A while LDPE is very transparent and appears bright and PET and Kraton are dark in B.

always the danger of inducing artifacts associated with the staining process and the possibility of misinterpretation due to its non-linearity. These drawbacks of staining were part of the motivation to develop NEXAFS imaging at beamline X1A and the initial demonstration [11] involved a polymer blend of a random copolymer of polystyrene and styrene–acrylonitrile (PS-*r*-SAN) and polypropylene (PP). Subsequent to this and other demonstrations [25], researchers have started to investigate a variety of multicomponent polymer blends with the X1-STXM. As an example, we show the work of Liu et al. [26], who investigated the morphology of an elastic ternary blend of poly(ethylene terephthalate) (PET), low-density polyethylene (LDPE) and maleated Kraton with the X1-STXM. Of particular interest is the distribution of the Kraton, a rubbery component, and more specifically whether the Kraton is also located at the PET/LDPE interface or only inside the LDPE domains. Careful inspection of the micrographs in Fig. 5 clearly suggests that Kraton is indeed also present at the PET/LDPE interface. The features in the lower right-hand corner of this figure make this particularly obvious: dark domains are touching each other (Kraton around the LPDE domain) in Fig. 5(A), while by comparison the LDPE domains are sharply delineated and separated in Fig. 5(B). The interpretation of electron micrographs of stained samples of these materials yielded ambiguous results concerning the distribution of Kraton.

Another complex polymer system shown as an illustration here was investigated by Sloop et al. [27]. The polycarbonate/acrylonitrile–butadiene–styrene blends investigated are complex mixtures consisting of three polymeric components, polycarbonate (PC), styrene–acrylonitrile (SAN) copolymer, and SAN copolymer grafted onto polybutadiene in latex form (SAN-*g*-PB). They also contain small amounts of titanium oxide. These materials are extensively utilized, for example, in computer and terminal housings and enclosures. Sloop et al. are interested in how these materials behave if they were to be repeatedly recycled and what effect it would have on the morphology and if there would be compositional changes involved. NEXAFS micrographs delineating the nitrile distribution in an unrecycled material are shown Fig. 6. In Fig. 6(A), the SAN appears an intermediate gray, while the PB is very bright. Fig. 6(B) shows the SAN to appear as the darkest phase. The SAN is thus shown to accumulate at the interface between the continuous PC phase and the dispersed

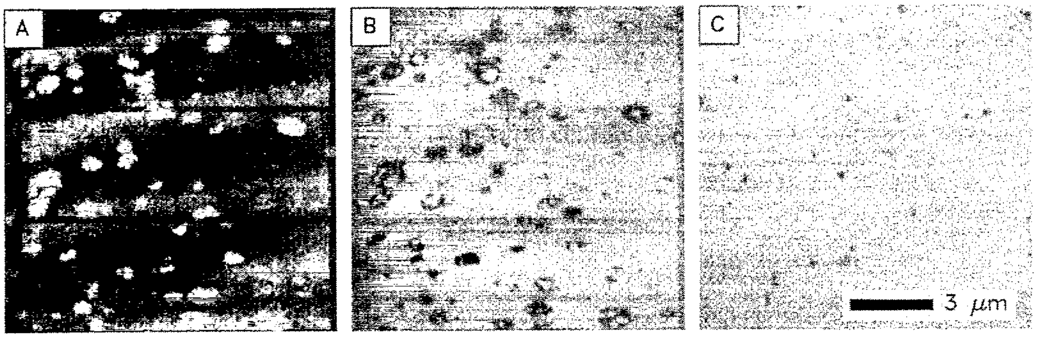

Fig. 6. NEXAFS images of polycarbonate/ABS blend acquired at (A) 285.43 eV, (B) 286.55 eV and (C) 282 eV. The brightest features in A are predominantly polybutadiene (PB), while the darker areas in B are regions with high nitrile concentrations (SAN) that typically enclose the PB particles. Micrograph C delineates TiO_2.

SAN-*g*-PB particles. Some free SAN also appears to be in the PC matrix, not associated with the SAN-*g*-PB. The titanium oxide can be located and emphasized in images acquired below the carbon edge (Fig. 6(C)) and is typically inside or in close proximity to the SAN/SAN-*g*-PB agglomerates.

Naturally, other polymer blends where the polymers exhibit unique spectral signatures are candidate materials for characterization with NEXAFS microscopy.

4.2. Phase-separated polymeric systems with phases visible with other techniques

The above-discussed materials contain relatively well-defined polymer components and are expected to have reasonably well-separated phases. The objective is to identify where the various components are. In order to find the photon energy with the most specific contrast for a particular polymer, one typically acquires reference spectra of the polymers of interest. A complementary problem where X-ray microspectroscopy can make meaningful contributions is when various phases segregate during synthesis and processing of polymers (or other materials) and the chemical composition of the phases has to be ascertained with microspectroscopy. The processing-dependent phase separation is at times the preferred, at other times an unwanted, characteristic of the material produced. In either case, understanding of the chemical composition is of great help in order to rationally modify the processing conditions and thus tailor the material properties.

In many cases of phase separation in polymer products, the morphology of the phases can be readily observed with electron microscopy (EM) techniques at high spatial resolution. However, just viewing the morphology is sometimes not sufficient to answer chemical questions about the phases formed. Electron energy loss spectroscopy (EELS) in an electron microscope can provide chemical information about polymer components in a blend [28], but one must be careful not to alter the chemistry of the sample due to relatively high radiation damage rates (see Section 4.6). Infrared microscopy would have, in most cases, the required chemical sensitivity, but it does not have sufficient spatial resolution to study submicron precipitates in polymer materials.

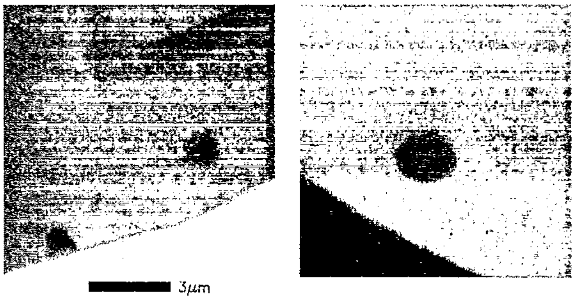

Fig. 7. X-ray micrographs of polyurethane precipitates acquired at a photon energy of 285.1 eV. These precipitates can be viewed in the electron microscope, but their chemical composition can only be assessed with spectroscopic techniques. Their size is too small for IR microscopy, and polyurethanes tend to be too radiation sensitive for the precipitates to be analyzed by EELS. For NEXAFS spectra of the matrix and the precipitate see Fig. 8.

A class of materials where one can view the morphology with EM, but where more specific chemical information is needed at high spatial resolution, is the polyurethanes. Methylene diphenyldiisocyanate (MDI) and toluene diisocyanate (TDI) based polyurethanes are produced in large quantities, with a world-wide production of about five million metric tons a year. The chemistry of polyurethanes is highly variable and complex. Some polyurethanes, such as slabstock polyurethane foams with high water content, can be high in polyureas. (The release of CO_2 during the formation of urea functionality is exploited to produce these foams.) Both MDI- and TDI-based materials can form precipitates during processing. The relative concentration of polyol, urea or urethane functionality in the precipitates might differ significantly from that of the matrix. The question of whether the precipitates are more urea or more urethane in character is of central importance in order to tailor the material properties. Fig. 7 presents micrographs of one of the various polyurethane materials investigated. It shows relatively sparsely distributed precipitates of moderate size. Based on core-excitation spectra of the small molecular analogs diisopropyl ether, phenyl urea and phenyl urethane recorded with EELS in the gas phase [29], analysis of the spectra acquired from the matrix and the precipitates (see Fig. 8) yields a composition of 39% polyol, 24% urethane and 37% urea in the matrix and 20% polyol, 52% urethane and 28% urea for the precipitates. The overall expected composition should

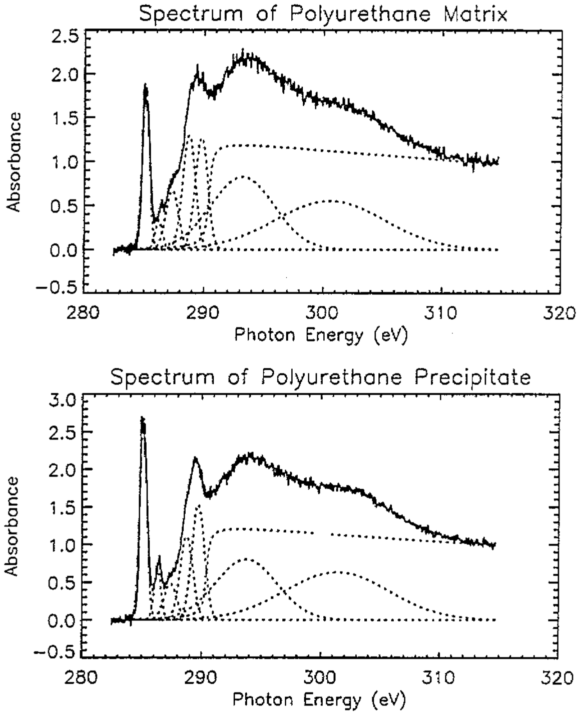

Fig. 8. NEXAFS spectra of precipitates and matrix of sample shown in Fig. 7.

be 40% polyol, based on the stoichiometric ratios of the starting material. Our analysis, at least for this component, comes very close, given the fact that the matrix provides by far the largest bulk of the material. However, at this point we do not have a true independent means of assessing systematic errors for the urea and urethane functionalities in this particular analysis and it furthermore depends strongly on the model analogs selected. It turns out that while IR and NMR spectroscopy and other methods can provide some complimentary information on chemical composition of the bulk materials, they cannot provide additional information on the urea/urethane ratio due to peak overlap and the inability to get the materials into solution. We are thus in the process of systematically determining the sensitivity of NEXAFS to urea and urethane functionalities by acquiring NEXAFS spectra of specially prepared model polyurethane polymers, polyols and polyurea [30], since the model polymers should be much better analogs than the molecules. Many of these oligomeric and polymeric model materials are difficult to prepare and to handle (liquids and small flakes), and the ability to support them on electron microscope grids and to utilize the microspectroscopic capability of the X1-STXM has greatly helped in being able to acquire spectra from these materials. We show as an example a polyurea model compound supported on a holey carbon grid in Fig. 9. This material consisted of fragments about 2 μm in size. The X1-STXM is then used to focus on one these fragments to acquire an energy scan of the sample. The micrographs in Fig. 9 also provide a good example of how open areas in the sample can be used for an I_0 energy scan. The X1-STXM beam is simply directed on any of the many open areas. Spectra of several model polyurethane/urea compounds are shown in Fig. 10. The spectral differences in the carbonyl region (288–289 eV) clearly indicate that we are able to differentiate urea from urethane functionalities and we can now reanalyze the spectra acquired from the various precipitates based on this different set of model compounds and model spectra.

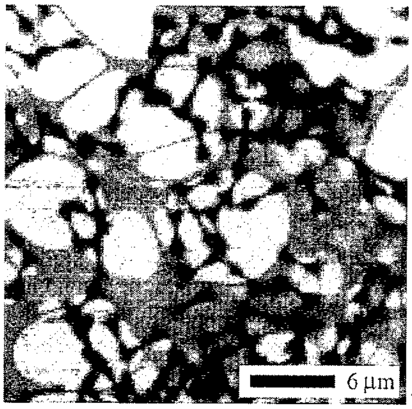

Fig. 9. X-ray micrographs of a model polyurea that formed fragments that could be supported on lacey carbon films. The X1-STXM is utilized to focus on one of these fragments lodged over a hole to acquire a NEXAFS spectrum.

4.3. Phase separation and morphology not previously observed

Another class of STXM application involves the detection of phases in polymeric materials that might have formed during processing but could not be viewed with other techniques. In this case, STXM can then be used to view the morphology for the first

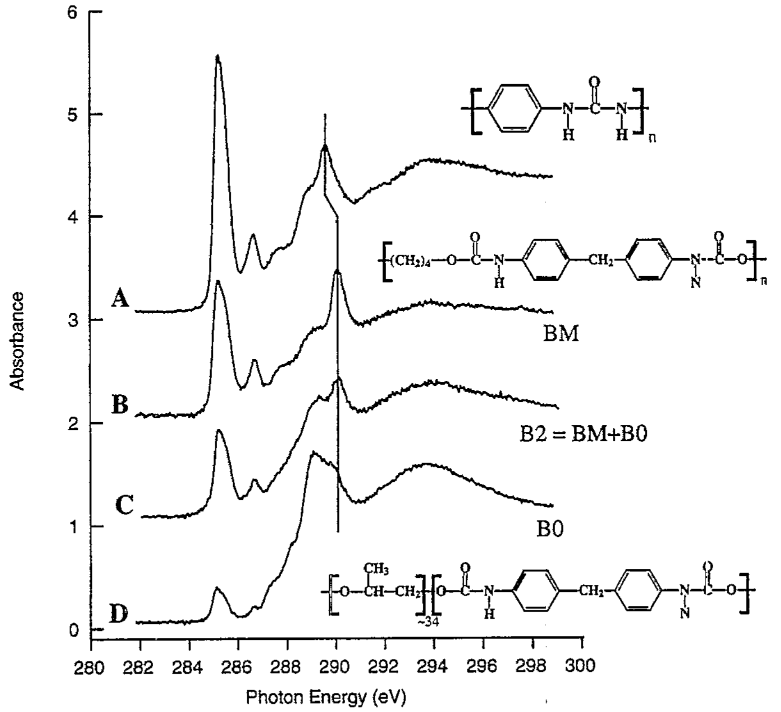

Fig. 10. NEXAFS spectra of various polyurethane model polymers with the chemical structure as indicated. B2 is a model polymer made of components of BM and B0 but does not equal BM + B0 exactly.

time and, if it is desired, to analyze the chemical composition of the various phases. We have, for example, investigated the phase morphology of a liquid crystalline polyester (LCP) based on several aromatic monomers. EM and differential scanning calorimetry (DSC) indicated the existence of phase separation in certain materials based on this polyester but not in others. However, the results were not conclusive and these techniques did not have the required sensitivity to determine how many phases are present in these materials and whether these phases are chemically distinct or whether the EM and DSC observations are solely due to differences in crystallinity. Two materials based on this LCP were processed differently (melt-screened versus unscreened) and thin sections were subsequently examined with the X1-STXM. The melt-screened material was extruded with a screening pack designed to filter particles larger than 150 μm. In the unscreened material, NEXAFS microscopy revealed an unusual morphology and determined that the unscreened material had four chemically distinct phases. As an illustration of the texture of this material, we show micrographs acquired at photon energies of 285, 286, 286.8 and 281.8 eV (Fig. 11(A), Fig. 11(B), Fig. 11(C) and Fig. 11(D) respectively). Micrograph 11(A) emphasizes aromatic functionalities in the sample, and a discontinuous phase with domains smaller then 100 nm, as well as a continuous phase enclosing elliptical bodies with dimensions of a few microns, is clearly discernible. Fig. 11(B) reverses the contrast between the larger features, while there is virtually no contrast between the small features at this energy due to the particular NEXAFS cross-section for this chemical composition. Fig. 11(C) is acquired at a photon energy that has only residual chemical sensitivity and is a mixed ''density/thickness/chemistry map'' that most closely resembles the electron micrographs of this material (although none of the X-ray images closely resembled the electron micrographs due to the different contrast mechanism in the two techniques). Micrograph 11(D) is acquired below the carbon edge, and emphasizes elements other than carbon. Given the elemental constituents and

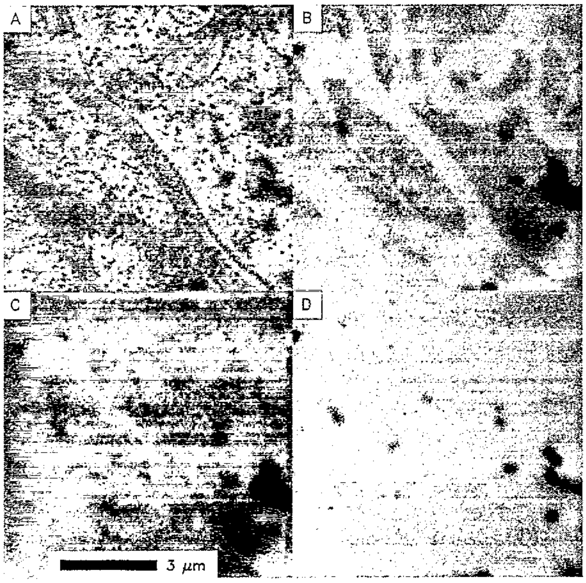

Fig. 11. Micrographs of the same region of a thin section of an aromatic liquid crystalline polyester imaged at a photon energy of (A) 285.0 eV, (B) 286.8 eV, (C) 296.2 eV and (D) 281.8 eV.

the low level of metal contamination in this polymer as determined by other techniques, the dark features in Fig. 11(D) are regions interpreted as rich in oxygen, presumably from carbonyl functionalities. This complex morphology based on different chemical compositions was only observed in the unscreened material and was completely absent in the screened material. The images thus clearly demonstrate the dependence of the morphology of these material on the processing route employed.

4.4. Linear dichroism microscopy of Kevlar® fibers

In the preceding applications we have generally assumed, guided by knowledge about the materials from other techniques, that the materials are either isotropic within the sample volume probed or, if not truly isotropic, that orientational order on a small scale is averaged out over the volume probed with the STXM and that there are no polarization-dependent effects. In general, the polarization dependence of NEXAFS spectra from oriented materials is a well-documented and understood phenomenon [14]. The resulting linear dichroism in transmission microscopy, in which the absorbance depends on the orientation of the sample, can be utilized to assess orientation and the degree of orientational order in materials. Since the X1 undulator radiation is linearly polarized, orientationally ordered systems can be characterized down to the size scale of the spatial resolution of the X1-STXM. We have obtained, for example, a quantitative determination of the relative lateral orientational order of various poly(*p*-phenylene terephthalamide) Kevlar® fiber grades. The internal structure of these technologically important, high crystallinity fibers is highly complex and certain aspects of its structure are still subject to debate. In particular, an accurate measure of the lateral orientational order of these fibers is still elusive. Micrographs of thin sections (45° with respect to the fiber axis) of these fibers exhibit a "butterfly" pattern when imaged at photon energies specific to certain chemical functionalities. This pattern reflects the average lateral orientation of these groups and shows, for example, that the average aromatic ring planes and carbonyl groups are pointing radially outwards [31]. The observed difference of the contrast of this pattern in micrographs from different fiber grades (Fig. 12) reflects the relative degree of orientational order and follows the trends of the relative crystallinity of these

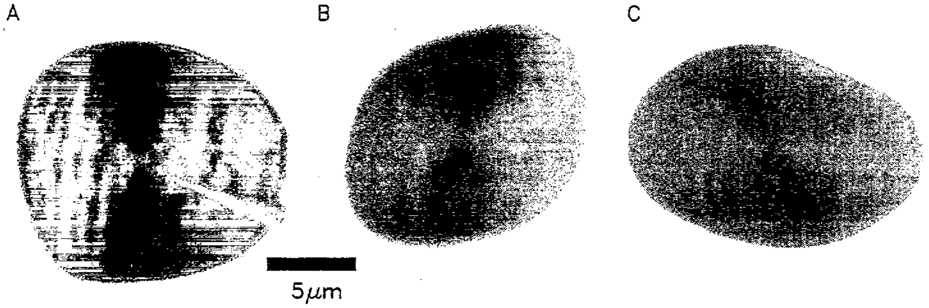

Fig. 12. X-ray micrographs of thin sections of Kevlar® 149, 49 and 29 fiber grades acquired at a photon energy of 285.1 eV.

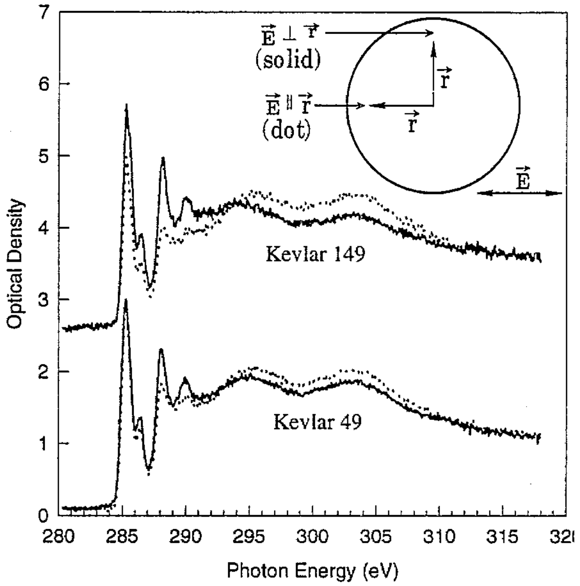

Fig. 13. Spectra from perpendicular (solid) and parallel (dot) locations of Kevlar® 149 and Kevlar® 49 fiber thin sections. The larger difference between the Kevlar® 149 spectra with respect to the Kevlar® 49 spectra reflects the higher degree of radial orientation in Kevlar® 149. Inset shows locations of parallel and perpendicular data acquisition points within the cross-section.

fibers (Kevlar® 149 is largest and Kevlar® 29 is smallest [32]) even though these parameters are not directly related.

After the initial demonstration of sensitivity to orientation in the imaging mode, we acquired NEXAFS spectra in the microspectroscopy mode providing quantitative information about the orientation of these fibers. We acquired carbon K-edge absorption spectra from several azimuthal angles 1–2 μm from the fiber edge. The photon absorbance and optical density is found to be, as expected, a function of azimuthal angle due to the radial symmetry of functional groups in these fibers (see Fig. 13). The differences in optical density for the various spectral features are extracted by simultaneously least squares fitting all spectra from the same fiber. We define a spectral feature-specific molecular "orientation parameter" OP as the difference in optical density of a specific spectral feature in the spectra from locations with the radial position vector parallel and perpendicular to the polarization vector (see inset Fig. 13) divided by the sum of these optical densities [33]. Using this OP, we have found average values of 0.20 for Kevlar® 149, 0.12 for Kevlar® 49 and 0.09 for Kevlar® 29 for the spectral peak dominated by the carbonyl functionality at 287.8 eV. Ratios of this parameter between fiber grades reflect the relative degree of radial orientational order. The ratios found for the three lowest energy peaks are similar to those found for the carbonyl peak. On average, Kevlar® 149 is 1.6 and 2.3 times more radially orientationally ordered than Kevlar® 49 and Kevlar® 29, respectively [33].

After correcting for non-perfect linear polarization, the orientation of the various functional groups in the unit cell, and allowing for a possible rotation of microcrystallites, we will be able to extract the absolute degree of lateral orientation within these fibers by utilizing the OP from several spectral features. Special care will have to be exercised for spectral features in the 287–290 eV energy range as they have contributions from more than a single functional group. In this application, it would be of great value to study the dependence of the carbonyl group at the oxygen K-edge, where its associated spectral feature is well isolated compared to the carbon edge feature that has underlying spectral intensity from C–H σ^* transitions and C–R π^* transitions. Nitrogen NEXAFS spectra might also be of great value [30].

4.5. Other STXM NEXAFS applications

Additional work to that presented here has been performed on various other polymeric systems. Mitchell et al. [34] have utilized the X1-STXM to investigate structured latex particles, Liu et al. [26] have studied the miscibility of poly(ethylene terephthalate) (PET) and polyarylate (PAR) in PET/PAR polymer blends, and Zimba et al. [35] have investigated layered polymers or polymer laminates and diffusion of polymers at interfaces. In addition, Zhang et al. [36] have utilized the X1-STXM to develop exposure strategies for PMMA resists.

So far, we have discussed STXM applications to synthetic polymers and the spatial location and orientation of components and functional groups in these polymeric materials. NEXAFS microscopy is also capable of providing information for complex systems such as biological samples. Zhang et al. [37] first showed that NEXAFS microscopy can be used to discriminate the DNA and protein components of Chinese hamster ovary cells and, subsequently, in the first quantitative application of NEXAFS microscopy to a biological system, Zhang et al. [38] have mapped the relative abundance of DNA and specific proteins (protamine 1 and protamine 2) in various mammalian sperm heads and measured the overall DNA to protein ratio. These results have provided new information about the packaging of sperm DNA by protamine 1 and 2.

Even more complex large molecules and polymers than the ones discussed so far occur in organic geochemistry. While this might present some challenges for the technique, it is still possible to provide a wealth of new information for complex systems such as coal, organic-rich sediments and ancient wood, and provide details about the chemical modification of these materials over time. For example, Cody et al. have investigated the microheterogeneities in a high volatile A bituminous coal [39] and a subbituminous coal [40], performed in situ analysis of sporopollenin/sporinite in a rank-variable suite of organic-rich sediments [41], and have investigated the photochemical alteration of geological organic matter [42]. Due to the fact that NEXAFS is specific to the local environment of the core hole that is created, aggregate averages of ''building blocks'', such as aromatics, hydroxylated aromatics, methyl/methylene carbon and carboxylic carbons, can be assessed in these studies.

In other applications, Chapman et al. [43] have utilized the analytical capabilities of the X1-STXM to characterize interstellar dust and micrometeorites, while Buckley [44] is utilizing carbon NEXAFS to differentiate organic components of osteoporotic bone from the embedding material.

4.6. Comparison of NEXAFS microscopy with EELS microscopy

The electronic structure information provided by NEXAFS spectroscopy can also be obtained with electron energy loss spectroscopy (EELS) under dipole selection rule conditions. EELS, which is extensively utilized in the gas phase [45] to characterize the electronic structure of small molecules, can also be performed in an electron microscope with an energy filter. This results in a general material analysis tool with high spatial resolution capabilities [46,47]. A comparison between NEXAFS and EELS microscopy and the relative damage associated with each technique has been performed recently by observing near edge spectral changes in PET as the polymer gets increasingly damaged [15]. In this study the EELS spectra were recorded in a scanning transmission electron microscope (VG HB 501) equipped with a field emission source and a parallel detection electron spectrometer (Gatan model 666). The X-ray data were recorded with the STXM at the NSLS. The EELS data were acquired at 100 K to reduce radiation damage, while the NEXAFS data were acquired at room temperature. Generally, the data acquired with NEXAFS microscopy provide more spectral detail due to better energy resolution. They also required a lower radiation dose for a given spatial resolution. As a rule of thumb, it was calculated that the STXM-NEXAFS technique has a 500-fold advantage over EELS in terms of the radiation sensitivity for acquisition of near edge spectra given the specific conditions used. Much of this advantage can be readily understood in that, in transmission NEXAFS, most core excitations result in a usable signal, while in EELS many excitations, particularly excitations of valence electrons, add dose to the sample but do not provide core edge signal. Additional advantages of NEXAFS microscopy over EELS include the above-described easy, in situ energy calibration with CO_2 and that it does not have to be performed in a high vacuum or at cryogenic temperatures.

5. SPEM performance and applications

While during the recent past many more spectromicroscopy experiments have been performed with the X1-STXM, the first X-ray spectromicroscopy experiments at X1 were actually performed with the X1-SPEM-I, the first-generation scanning photoemission microscope at X1A. Although it has worked well for proof-of-principle experiments, this device had poor energy resolution ($>$ 4 eV), as well as poor analyzer acceptance. Since it was apparent that substantial improvements in the performance could be achieved with the incorporation of a commercial hemispherical sector analyzer (HSA) with multichannel detection [48–50], the X1-SPEM-I has performed only a limited number of experiments [50]. During the past years, Ko and co-workers [21,51] constructed and commissioned the second-generation SPEM (X1-SPEM-II) of which the first phase upgrade, which included the installation of a vastly improved spectrometer and a more flexible zone plate mounting hardware, was recently completed.

5.1. Description of the X1-SPEM-II

The basic operating principle of the X1-SPEM-II is centered on the ability to focus the monochromatized X-ray beam from the X1 undulator to a microprobe through the deployment of a high-resolution zone plate (ZP) in complete analogy to the X1-STXM (see schematics in Figs 2 and 3). Photoelectrons emitted from the surface are then analyzed by an HSA and XPS spectra from the small illuminated region can be acquired. With the HSA set to monitor a particular spectral range and feature, the specimen may be scanned to form images. High-throughput XPS capabilities are achieved with a Perkin-Elmer HSA (model 10-360) equipped with an OMNI-II small-area lens modified for high transmission and a multichannel detector (MCD, 16 channels). Since the photoelectrons are energy dispersed in the exit plane of the HSA, the use of an MCD allows us to monitor photoelectrons of different kinetic energies simultaneously. A total of 16 XPS images can thus be acquired in a single mechanical raster scan.

In spite of strong competition from imaging spectromicroscopes, scanning instruments will always have certain advantages. These include:

1. The option of detailed analysis of preselected small spots on the surface (photoelectron spectra, absorption spectra, photon-stimulated desorption studies) while not exposing the uninvestigated areas to the potentially still-damaging X-ray beam.
2. Various signal channels, such as photoelectrons of preselected energy, NEXAFS/XANES in fluorescent, total electron and Auger electron yield, and luminescence. For thin samples the transmitted flux can also be utilized [52,53]. Several of these signals cannot be provided in charged particle imaging devices. In a scanning microscope, some of these signals can in principle also be monitored simultaneously.
3. In scanning devices, the spatial resolution and detection efficiency in a given operating mode are not coupled. This will, in particular, facilitate quantitative XPS analysis.
4. Scanning microscopes can also be better utilized to investigate highly corrugated surfaces.

In the future, some of these advantages might be somewhat eroded as ever more powerful electro-optical imaging systems are developed.

5.2. SPEM applications to tribological surfaces

After the initial commissioning of the X1-SPEM-II we started experiments on tribological surfaces. The study of rubbed and worn surfaces, particularly when generated in a lubricant with additives, almost always demands the use of microcharacterization methods. Traditionally, SEM, Auger and standard XPS methods have been used to characterize the surface morphologies and compositions which are created in tribo-contacts. More recently, atomic force microscopy/ lateral force microscopy (AFM/LFM) has been used to view surface textures, relative frictional properties and adsorbate molecular structures on the wear surfaces [54].

In one method of controlled fabrication of tribological surfaces, wear scars are produced by a rotating steel cylinder pressed against a carbon steel block in the presence of certain reference lubricants. A line contact is formed and the cylinder wears out a shallow scar about 1 mm × 7 mm in size (see schematic in Fig. 14). A reacted or deposited layer typically tens to hundreds of nanometers thick forms on the surface with the use of lubricant additives [55]. These reacted

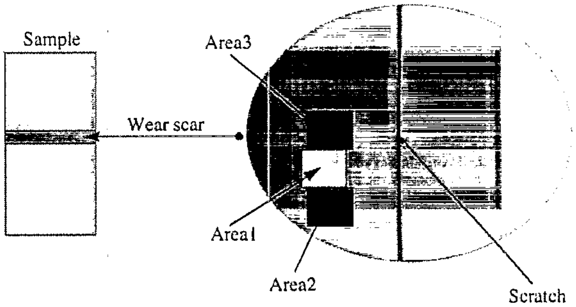

Fig. 14. Schematic of wear scar about 7 mm × 1 mm in size on the surface of a carbon steel block. Data presented in Figs 15 and 16 were acquired from area 1 within the wear scar as indicated. The scratch was utilized to more readily focus the sample.

layers play a dominant role in the prevention of wear and strongly influence the frictional properties of the system. The surface reaction layers are often completely inorganic, composed of phosphates, sulfides and oxides, but may also include organic polymeric components. The composition of such reaction layers, both elemental and chemical, will vary from region to region within a contact as a function of local contact pressure, temperature and sliding velocity. Because of the nature of tribo-contacts, the highest features (asperities) on a surface will experience higher temperatures, pressures and more wear than the ''valleys''. These contact differences lead to compositional differences also at the scale of the asperities, which are viewable in the near-micron size range with various complementary characterization techniques.

In the search for fuel-efficiency enhancing lubricant additives, organomolybdenum compounds have recently found significant use. Standard XPS has been used to show that the ratio of molybdenum sulfides to oxides on the surface is an important indicator of performance. While the effectiveness of various organomolybdenum compounds has seen much empirical testing, little is known about the structure/function relationships of compound type to performance. We thus started to study the distribution of the reaction-layer molybdenum species as a function of additive type and tribo-contact conditions, and investigated several wear scars. As a comparison, we have also investigated reference wear scars without molybdenum species. The wear scar presented here as an example has a molybdenum-containing reaction layer. The sample was lightly Ar sputter-cleaned to remove most of the carbon and other contaminants. The regions indicated in Fig. 14 have been imaged and survey spectra were acquired from a variety of areas less than 1 μm in size. A subset of the data of area 1 is shown in Fig. 15, in which micrographs delineate the S, P, Mo and Fe concentrations at this location. These maps were produced by averaging the central MCD channels corresponding to the photoemission peak and by subtracting the average of the outermost MCD channels. While this is not a perfect background subtraction, these images are at least semiquantitative and are only intended to give an appreciation of the variations that can be observed. The more telling aspect of this feasibility study is conveyed by the spectra acquired. Spectra of the nominal locations 1–4 in Fig. 15 are presented in Fig. 16. Clearly, the elemental concentration can vary significantly. There are regions with high concentrations of Mo and S, regions that are almost devoid of Mo and S, but rich in P, as well as other combinations. The most interesting aspect, even with the low-energy resolution of about 4 eV and the survey nature of the spectra, is the fact that we could observe that both the Mo and Fe exhibit significantly different spectral lineshapes, reflecting different oxidation states and chemical compounds. While it is too early to draw definitive conclusion about the precise species and composition at this point, we have observed chemical differences that are well within the spatial resolution of the X1-SPEM-II and higher resolution spectra of the specific elements of interest should be able to yield conclusive answers as to what the precise chemical nature of the local reaction layer is.

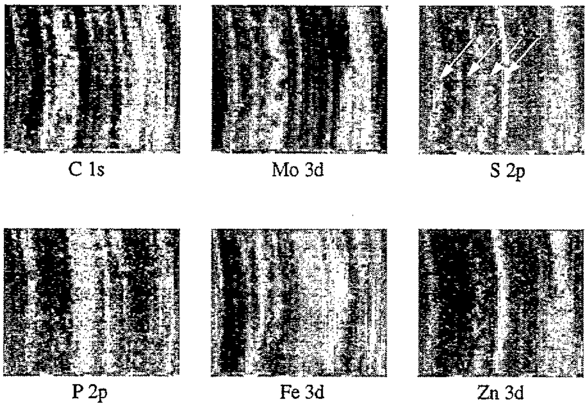

Fig. 15. C, S, P, Mo, Zn and Fe images (area 1 as indicated in Fig. 14: images are 75 × 75 pixels, 3 × 2.5 μm, 600 ms dwell). Some of the contrast observed might be due to differences in surface roughness present on these surfaces and observable by AFM/LFM.

Besides the spatial resolution of the X1-SPEM-II there are several additional aspects of this synchrotron radiation source-based instrument that facilitate these particular studies. The tunability of the photon energy can be utilized, for example, to excite with a photon energy below the oxygen K-edge and therefore the spectrum is free of the oxygen Auger background. In addition, at these low energies the S 2s peak is much reduced compared to its intensity with conventional laboratory sources. This is of great advantage because the S 2s level interferes with the Mo 3d in conventional XPS. This generally complicated the

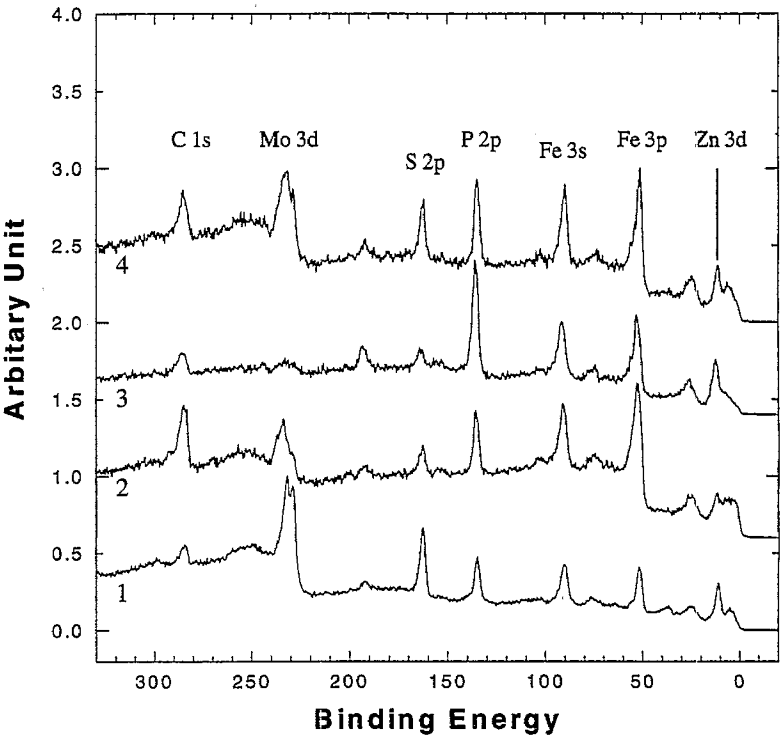

Fig. 16. Spectra from various locations along the wear scar illustrating compositional variations of the reaction layer. Both large elemental variations as well as changes in the Mo 3d and Fe 3p line shapes reflecting different oxidation states could be readily observed. (Nominal locations 1–4 of the wear scar shown in Fig. 15.)

analysis and interpretation of chemical shifts of the Mo spectral features which is rather crucial for a complete analysis. Even with the limited energy resolution due to the present beamline, interesting observations regarding the chemical and elemental composition could be made. The present results will guide further experiments with these kinds of samples once the new beamline is in operation.

6. Conclusions and future perspective

We have presented an overview of the spectromicroscopy activities with the X1-STXM and the X1-SPEM at beamline X1A and illustrated some of their applications. The X1-STXM in particular has produced a wealth of information on polymeric systems with an energy resolution of about 0.3 eV and a spatial resolution of up to 30–50 nm. X1-SPEM progress has been slower, hampered by its location on a branchline that shared a single grating with the branchline supporting the X1-STXM which has always been the major program at X1A. Initially, this arrangement has worked well because the X1-STXM has been operating at a single fixed energy near 350 eV, which provides an energy for SPEM operation in the vicinity of 700 eV. Recently, with the advent of NEXAFS microscopy with the X1-STXM and the many experiments that are performed in this operating mode, the relative arrangement between the X1-STXM and X1-SPEM has changed significantly. It is thus somewhat ironic that the success of increased NEXAFS activity with STXM came at the expense of the original spectromicroscopy program at X1A. Fortunately, two separate branchlines with independent energy and energy resolution control are presently being installed at X1A. This effort will improve the capabilities for both STXM and SPEM substantially. While there has not been much progress towards improved zone plates in the last few years from the groups associated with the X1A program, this situation might soon change as the Center for X-ray Optics at Lawrence Berkeley National Laboratory is installing a state-of-the-art electron lithography facility expressly for zone plate fabrication. A collaborative effort between Stony Brook and Lucent Technologies Bell Laboratories has already fabricated 30 nm outer zone width zone plates of 80 and 160 μm diameter using a commercially available *e*-beam lithography system [56]. One can thus hope that zone plate technology available for the X1A program is going to improve further and that the spatial resolution of the X1-STXM can be pushed below 30 nm. The X1-SPEM should achieve a resolution of about 50 nm in the next few years.

Acknowledgements

We would like to thank our colleagues of the Stony Brook X-ray microscopy group who have constructed and who maintain the X1-STXM and who have participated in the initial NEXAFS experiments. In particular, we thank C. Jacobsen, X. Zhang (now at Harvard), S. Wirick, and H. Chapman (now at LLNL). Particular thanks are due to C.-H. Ko (SUNY@Stony Brook, now at SRRC, Taiwan) for the construction of the X1-SPEM-II and S. Hulbert and E. Johnson from NSLS for their help with the X1-SPEM-II. The zone plates have been provided by E. Anderson and D. Attwood from CXRO and have been produced in a collaboration between CXRO and IBM. We would also like to thank B. Hsiao, S. Subramoney, B. Wood and I. Plotzker from DuPont, G. Young, G. Mitchell and W. Lidy, from Dow Chemical, C. Sloop from IBM, D.-J. Liu, S.C. Liu, J. Chung, J. Marti and A. Monisera from AlliedSignal, R. Fornes and R. Gilbert from North Carolina State University, D. Leta, R. Polizzotti and S. Cameron from EXXON Research and Engineering, and P. Schmitz from Ford Motor Company for providing samples and guidance with some of the experiments, and for sharing their knowledge about the provided materials. C. Jacobsen kindly read the manuscript and made very valuable suggestions. H.A. is supported by a National Science Foundation Young Investigator Award (DMR-9458060), a DuPont Young Professor Grant, and grants from The Dow Chemical Corporation and EXXON Research and Engineering. Operation and development of the X1A beamline and its instrumentation is supported by the DOE under grant # FG02-89ER60858. The NSLS is supported by the Department of Energy, Energy Research, Office of Basic Energy Sciences.

References

[1] J. Kirz, R. Burg, H. Rarback, Annals of the New York Academy of Sciences 342 (1980) 135.
[2] J. Kirz, H. Ade, C. Jacobsen, C.-H. Ko, S. Lindaas, I. McNulty, D. Sayre, S. Williams, X. Zhang, M. Howells, Review of Scientific Instruments 63 (1992) 557.
[3] C. Jacobsen, S. Williams, E. Anderson, M.T. Brown, C.J. Buckley, D. Kern, J. Kirz, M. Rivers, X. Zhang, Optics Communications 86 (1991) 351.
[4] J.M. Kenney, C. Jacobsen, J. Kirz, J. Rarback, F. Cinotti, W. Thomlinson, R. Rosser, Schidlovsky, Journal of Microscopy (1985) 321.
[5] J. Kirz, C. Jacobsen, M. Howells, Quarterly Reviews of Biophysics 28 (1995) 33.
[6] H. Ade, J. Kirz, H. Rarback, S. Hulbert, E. Johnson, D. Kern, P. Chang, Y. Vladimirsky, in: D. Sayre, M. Howells, J. Kirz, H. Rarback, (Eds.), X-Ray Microscopy, Springer, Berlin, 1988, p. 280.
[7] H. Ade, J. Kirz, S. Hulbert, E. Johnson, E. Anderson, D. Kern, Applied Physics Letters 56 (1990) 1841.
[8] H. Ade, C.H. Ko, E. Anderson, Applied Physics Letters 60 (1992) 1040.
[9] G.R. Harp, Z.L. Han, B.P. Tonner, Physica Scripta T31 (1990) 23.
[10] G.R. Harp, Z.L. Han, B.P. Tonner, Journal of Vacuum Science Technology 8 (1990) 2566.
[11] H. Ade, X. Zhang, S. Cameron, C. Costello, J. Kirz, S. Williams, Science 258 (1992) 972.
[12] W. Ng, A.K. Ray-Chaudhuri, S. Liang, S. Singh, H. Solak, J. Welnak, F. Cerrina, G. Margaritondo, J.H. Underwood, J.B. Kortright, R.C.C. Perera, Nuclear Instruments & Methods A 347 (1994) 422.
[13] E. Bauer, C. Koziol, B. Lilienkamp, T. Schmidt, Journal of Electron Spectroscopy and Related Phenomena, this issue.
[14] J. Stöhr, NEXAFS Spectroscopy, Springer-Verlag, Berlin, 1992.
[15] E.G. Rightor, A.P. Hitchcock, H. Ade, R.D. Leapman, S.G. Urquhart, A.P. Smith, G. Mitchell, D. Fisher, H.J. Shin, T. Warwick, Journal of Physical Chemistry, 101 (1997) 1950.
[16] J. Kikuma, B.P. Tonner, Journal of Electron Spectroscopy 82 (1996) 53.
[17] D.A. Outka, J. Stöhr, J.P. Rabe, J. Swalen, H.H. Rotermund, Physical Review Letters 59 (1987) 1321.
[18] T. Ohta, K. Seki, R. Yokoyama, I. Morisada, K. Edamatsu, Physica Scripta 41 (1990) 150.
[19] C.C. Turci, S.G. Urquhart, A.P. Hitchcock, Canadian Journal of Chemistry 74 (1996) 851.
[20] S.G. Urquhart, A.P. Hitchcock, A.P. Smith, H. Ade, E.G. Rightor, J. Phys. Chem., 101 (1997) 2267.